Doping evolution of spin fluctuations and their peculiar suppression at low temperatures in $Ca(Fe_{1-x}Co_x)_2As_2$

A. Sapkota,[1,2] P. Das,[1,2] A. E. Böhmer,[1,2] B. G. Ueland,[1,2] D. L. Abernathy,[3] S. L. Bud'ko,[1,2] P. C. Canfield,[1,2]
A. Kreyssig,[1,2] A. I. Goldman,[1,2] and R. J. McQueeney[1,2]
[1] *Ames Laboratory, US Department of Energy, Iowa State University, Ames, Iowa 50011, USA*
[2] *Department of Physics and Astronomy, Iowa State University, Ames, Iowa 50011, USA*
[3] *Quantum Condensed Matter Division, Oak Ridge National Laboratory, Oak Ridge, Tennessee 37831, USA*

(Received 5 February 2018; revised manuscript received 13 May 2018; published 29 May 2018)

Results of inelastic neutron scattering measurements are reported for two annealed compositions of $Ca(Fe_{1-x}Co_x)_2As_2$, $x = 0.026$ and 0.030, which possess stripe-type antiferromagnetically ordered and superconducting ground states, respectively. In the AFM ground state, well-defined and gapped spin waves are observed for $x = 0.026$, similar to the parent $CaFe_2As_2$ compound. We conclude that the well-defined spin waves are likely to be present for all x corresponding to the AFM state. This behavior is in contrast to the smooth evolution to overdamped spin dynamics observed in $Ba(Fe_{1-x}Co_x)_2As_2$, wherein the crossover corresponds to microscopically coexisting AFM order and SC at low temperature. The smooth evolution is likely absent in $Ca(Fe_{1-x}Co_x)_2As_2$ due to the mutual exclusion of AFM ordered and SC states. Overdamped spin dynamics characterize paramagnetism of the $x = 0.030$ sample and high-temperature $x = 0.026$ sample. A sizable loss of magnetic intensity is observed over a wide energy range upon cooling the $x = 0.030$ sample, at temperatures just above and within the superconducting phase. This phenomenon is unique amongst the iron-based superconductors and is consistent with a temperature-dependent reduction in the fluctuating moment. One possible scenario ascribes this loss of moment to a sensitivity to the c-axis lattice parameter in proximity to the nonmagnetic collapsed tetragonal phase and another scenario ascribes the loss to a formation of a pseudogap.

DOI: 10.1103/PhysRevB.97.174519

I. INTRODUCTION

Understanding the interplay between structure, magnetism, and superconductivity (SC) in unconventional superconductors is a major theme of condensed-matter physics, and the 122-iron arsenide superconductors provide prominent examples of these phenomena [1–3]. The parent 122 compounds (AFe_2As_2, $A =$ Ca, Sr, Ba) are tetragonal (T) at ambient temperature and pressure, and consist of FeAs layers separated along the c crystalline axis. A structural phase transition into an orthorhombic (O) phase occurs upon cooling through a temperature T_S [4–6], which is accompanied by the onset of stripe-type antiferromagnetic (AFM) order below the Néel temperature T_N [2,7]. The AFM order is stripe type and characterized by an AFM propagation vector of $\boldsymbol{\tau}_{\text{stripe}} = (\frac{1}{2}\frac{1}{2}1)$, with respect to the high-temperature T unit cell [2,7]. SC appears in the presence of substantial spin fluctuations [2,7], after suppression of the AFM order by either chemical substitution [8–12] or pressure [13–17]. Thus the close proximity of AFM order and SC in these compounds and the presence of spin fluctuations in their SC states suggest an intimate relationship between the magnetism and SC. In particular, the overdamped and diffusive spin fluctuations present in the SC state are considered a necessary component of the SC pairing mechanism [18].

Among the members of AFe_2As_2, $CaFe_2As_2$ is unique. Its T-O structural and magnetic phase transitions are strongly first order [1,8,19]. Unlike $Ba(Fe_{1-x}Co_x)_2As_2$ [6,9], the first-order magnetostructural transition persists with electron doping in $Ca(Fe_{1-x}Co_x)_2As_2$ and effectively forbids the microscopic coexistence of AFM and SC phases [20], which is found in $Ba(Fe_{1-x}Co_x)_2As_2$ [9]. It also transitions to a collapsed tetragonal (cT) phase via either the application of modest pressure (the smallest among AFe_2As_2) [21,22] or by specific postgrowth annealing and quenching protocols [20,23]. The cT phase is characterized by a reduction in c of ≈9.5% [21] and quenching of the Fe magnetic moment, which results in the complete absence of AFM order and spin fluctuations [21,24,25]. The quenching of the Fe moment is associated with the formation of interlayer As-As bonds along c [24,26], which shows that strong magnetoelastic coupling is present.

It is unknown how these two magnetoelastic couplings affect the nature of the spin dynamics or SC. We address this question by (i) comparing the evolution of the spin dynamics of O-AFM $Ca(Fe_{1-x}Co_x)_2As_2$ with $Ba(Fe_{1-x}Co_x)_2As_2$, considering the strong first-order nature of the T-O transition in the former, and (ii) determining if the nearby cT phase has any influence on the spin dynamics. In particular, Ref. [27] shows that for certain compositions of T $Ca(Fe_{1-x}Co_x)_2As_2$, c strongly decreases with decreasing temperature. This provides a favorable situation for studying effects due to the coupling between the As-As interlayer distance and the magnetism by simply decreasing the temperature. In addition, the relevance of this magnetoelastic coupling in T $CaFe_2As_2$ has been indicated by the density functional theory (DFT) [24] and anomalies in the phonon spectrum of the T phase of $CaFe_2As_2$, which have been associated with the compound's proximity to the cT phase [28].

In this paper, we present results from inelastic neutron scattering (INS) experiments on coaligned single-crystal samples of $Ca(Fe_{1-x}Co_x)_2As_2$ with $x = 0.026 \pm 0.001$ and

0.030 ± 0.001. The $x = 0.026$ sample is orthorhombic and possesses stripe-type AFM order at low temperature, whereas the $x = 0.030$ sample remains T and is SC at low temperature. We first show that spin waves in the O-AFM state of $x = 0.026$ bear close resemblance to those for the O-AFM phase of $CaFe_2As_2$, except for a weakening of the interlayer exchange interaction. Second, we show that diffusive spin fluctuations, characterized by a short magnetic-correlation length and the presence of Landau damping, occur in the paramagnetic (PM) state for both $x = 0.026$ and 0.030. We find that diffusive spin dynamics may be absent for all values of x corresponding to the O-AFM phase at low temperatures, which appears consistent with the absence of a region of microscopically coexisting low-temperature AFM order and SC. Finally, we report a peculiar temperature dependence of the diffusive spin dynamics for $x = 0.030$, wherein the imaginary part of the dynamic magnetic susceptibility decreases upon cooling towards the SC state. We suggest that this is due to a reduction in the fluctuating Fe moment either because of the proximity to the cT phase or the opening of a pseudogap.

II. EXPERIMENTAL DETAILS

Single crystals of $Ca(Fe_{1-x}Co_x)_2As_2$ with $x = 0.026 \pm 0.001$ and 0.030 ± 0.001, as determined by wavelength dispersive x-ray spectroscopy, were grown using FeAs self-flux and annealed at $T = 400\,^\circ\mathrm{C}$, which ensured an ambient pressure T (uncollapsed) phase at all temperatures [20,29]. INS measurements were carried out on 10 and 14 coaligned single crystals, for $x = 0.026$ and 0.030, respectively. Each sample had a total mass of $\approx$1 g, and was aligned in the (H,H,L) scattering plane, with mosaics characterized by full widths at half maximum (FWHM) in rocking scans of $<1.3^\circ$. The $x = 0.026$ coaligned sample shows the magnetostructural transition over a range of $T_{\mathrm{S,N}} = 56$ to 73 K, and the $x = 0.030$ coaligned sample remains PM and becomes SC below $T_c = 13.5$ to 14.5 K. These two values of x were chosen so that measurements could be made as close to the phase boundary between the low-temperature AFM and SC states as practical, given the relatively large mass requirements for INS experiments. Figures 1(b) and 1(c) show magnetization data which illustrate the magnetostructural and superconducting transitions for $x = 0.026$ and 0.030, respectively. These data are for single crystals from the same batches used for the INS experiments.

INS measurements were performed on the ARCS spectrometer [30] at the Spallation Neutron Source at Oak Ridge National Laboratory, and samples were cooled using a closed-cycle He cryostat. Measurements were carried out with the incident neutron beam along c using various incident energies: $E_{\mathrm{i}} = 49.75$ meV for both $x = 0.026$ and 0.30 measured at $T = 20$ and 90 K, $E_{\mathrm{i}} = 49.75$ meV for $x = 0.030$ measured at $T = 6$ K, and $E_{\mathrm{i}} = 73.9$ and 238.4 meV for $x = 0.026$ measured at $T = 20$ K. Measurements were also made on the $x = 0.026$ sample at $T = 20$ K while rotating it about its vertical axis in 1° steps over a 145° range. For these measurements, $E_{\mathrm{i}} = 73.9$ meV.

Throughout the paper, we give the momentum transfer as $\mathbf{Q} = (H-K, H+K, L) = (2\pi/a)(H-K)\hat{\mathbf{i}} + (2\pi/a)(H+K)\hat{\mathbf{j}} + (2\pi/c)L\hat{\mathbf{k}}$ with respect to the tetragonal *I*4/*mmm* unit cell. At ~300 K, $c = 11.63$ Å for both concentrations, and $a = 3.91$ and 3.88 Å for $x = 0.026$ and 0.030, respectively. In our notation, the reciprocal-lattice vectors for stripe-type AFM order are $\mathbf{Q}_{\mathbf{stripe}} = (\frac{m}{2}, \frac{n}{2}, l)$ with m, n, and l odd integers. Data were visualized using the MSLICE [31] and HORACE [32] software packages. Incoherent nuclear scattering from a vanadium standard was used to normalize the data, and we report the dynamical structure factor $S(\mathbf{Q},E)$ in units of mbarn/sr meV f.u., where E is neutron energy transfer and f.u. is formula unit. The values determined using this method are accurate within 20%–30% of the actual values. Where possible, data have been averaged over symmetry-equivalent quadrants.

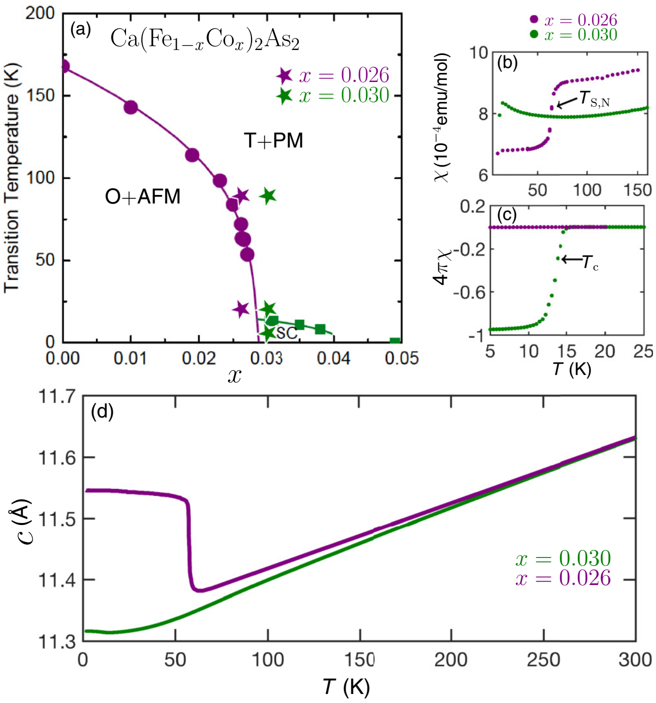

FIG. 1. (a) Phase diagram of $Ca(Fe_{1-x}Co_x)_2As_2$ annealed at $400\,^\circ\mathrm{C}$ showing the magnetostructural transition from the high-temperature tetragonal (T) and paramagnetic (PM) to the orthorhombic (O) and antiferromagnetic (AFM) phase, as well as the superconducting (SC) phase. Stars indicate the positions at which our INS measurements were performed. (b),(c) Magnetization data illustrating the T-PM to O-AFM transition at $T_{\mathrm{S,N}}$ for $x = 0.026$ (purple circles) and the superconducting transition at T_c for $x = 0.030$ (green circles). (d) Temperature dependence of the c lattice parameter for $x = 0.026$ (purple line) and 0.030 (green line). The c lattice parameters for the $x = 0.026$ and 0.030 samples at 300 K were obtained from the center of the (0,0,8) Bragg peak, measured with neutron diffraction. The temperature dependence plots in (d) were made by normalizing dilatometry data for $x = 0.027$ and 0.029 given in Ref. [27] to the value of c at $T = 300$ K for $x = 0.026$ and 0.030, respectively. An abrupt increase in c is seen for $x = 0.026$ at $T_{\mathrm{S,N}}$.

III. RESULTS

A. Spin waves in the orthorhombic-antiferromagnetic phase

Figures 2(a)–2(g) show INS spectra for the AFM phase of $x = 0.026$ at $T = 20$ K with $E_{\mathrm{i}} = 73.9$ meV, for either the incident beam along $\mathbf{c}$ [Figs. 2(a)–2(f)] or the sample being rotated about its vertical axis [Fig. 2(g)]. For the case of the

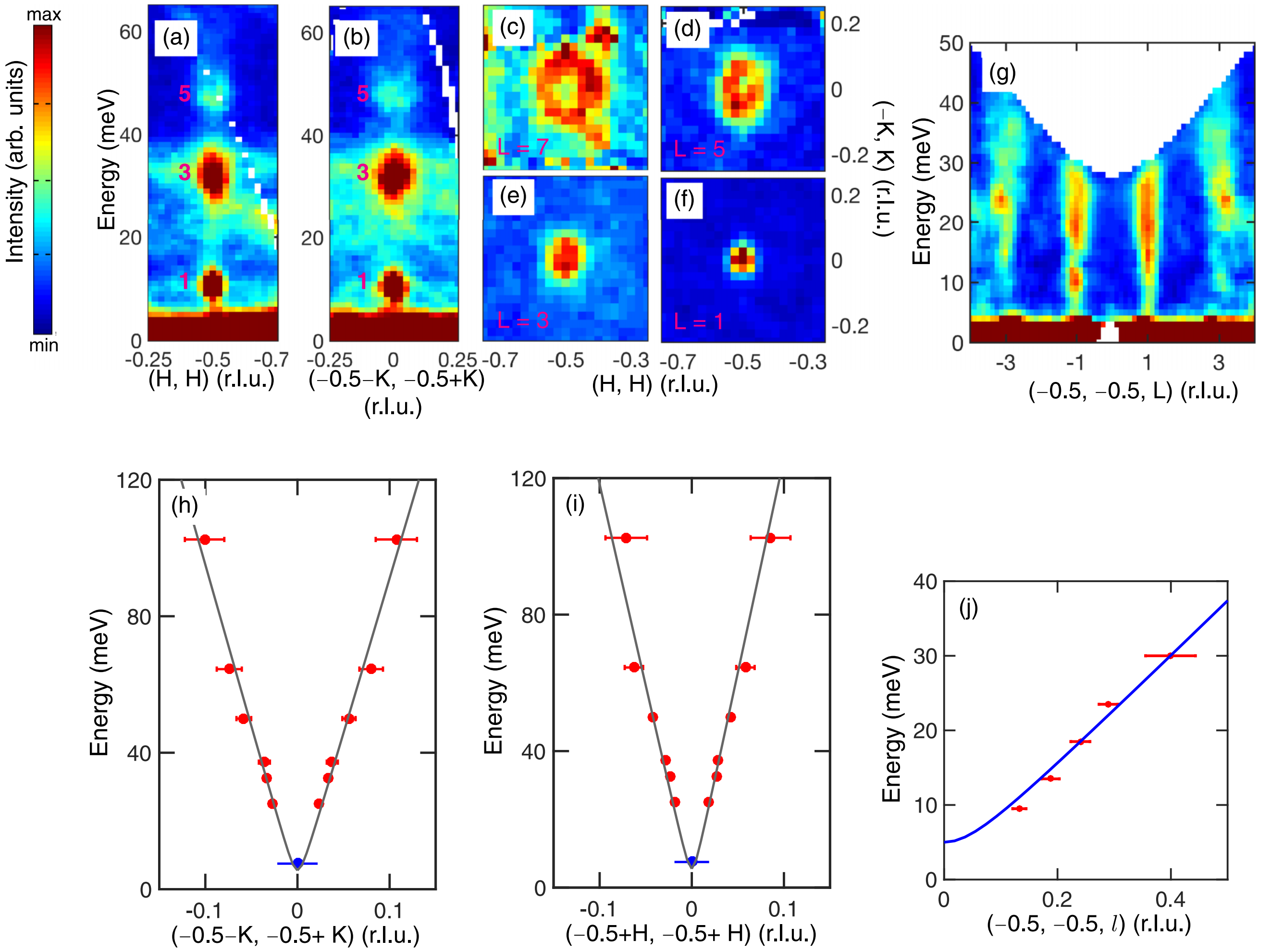

FIG. 2. Inelastic neutron scattering data for Ca(Fe$_{1-x}$Co$_x$)$_2$As$_2$, $x = 0.026$, measured at $T = 20$ K. (a) Energy dependence of the scattering along the $[H,H]$ [longitudinal (LO)] direction after averaging over a range of ±0.1 r.l.u. in the $[-K,K]$ [transverse (TR)] direction. (b) Energy dependence of the scattering along the TR direction after averaging over a range of ±0.1 r.l.u. in the LO direction. (c)–(f) Q (constant-energy) slices of the data obtained by averaging over $E = 59$–63 (c), 45–51 (d), 30–34 (e), and 8–12 meV (f). Data in (a)–(f) are for c fixed along the incident-beam direction, which couples E and L. Red numbers in (a) and (b) indicate odd values of L. (g) Energy dependence of the scattering along the $[0,0,L]$ direction after averaging over a range of ±0.05 r.l.u. for both the TR and LO directions. Data are from measurements made by rotating the sample about its vertical axis in 1° steps over a 145° range. (h)–(j) Spin-wave dispersion along the TR (h), LO (i), and $[0,0,L]$ (j) directions. Solid lines are fits to Eq. (1). Points in (j) show the half width at half maximum of peaks centered at (0.5, 0.5, 1, or 3), and the dispersion provides a lower bound for the spin-wave velocity along L.

incident beam fixed along **c**, L is coupled to E. Similar to CaFe$_2$As$_2$ [33], well-defined gapped spin waves with small damping originate from $\mathbf{Q}_{\text{stripe}}$ and steeply disperse along all three crystallographic directions. The Q (constant-energy) slices in Figs. 2(c) and 2(d) show the ringlike structure expected for nearly isotropic dispersion in the **ab** plane, with the small ellipticity being due to anisotropic spin-wave velocities in the $[H,H]$ [longitudinal (LO)] and $[-K,K]$ [transverse (TR)] directions.

To quantify the dispersion, we cut the Q slices in Figs. 2(c)–2(f) through $\mathbf{Q}_{\text{stripe}} = (-0.5, -0.5, L = 3,5,\ldots)$ along the LO and TR directions, and fit the resulting two peaks with Gaussian line shapes. The fitted peak positions are shown in the dispersion plots for the TR and the LO directions given in Figs. 2(h) and 2(i), respectively. For $L = 1$, only a single peak is found, which is fit to a Gaussian line shape, and the determined FWHMs for each direction are shown as blue symbols. Similarly, only a single peak is observed for Q cuts through the data in Fig. 2(g). In this case, Fig. 2(j) shows the half width at half maximum of the peak obtained by fitting a Gaussian line shape convoluted with the instrumental resolution. Details are given in the Appendix.

We fit the plots in Figs. 2(h)–2(j) using a dispersion model that considers anisotropic spin-wave velocities along the three orthogonal directions:

$$E(\mathbf{q}) = \sqrt{\Delta^2 + v_{\text{LO}}^2 q_{\text{LO}}^2 + v_{\text{TR}}^2 q_{\text{TR}}^2 + v_c^2 q_c^2}. \qquad (1)$$

Here, v_{LO}, v_{TR}, and v_c are spin-wave velocities along the LO, TR, and c directions, respectively, and $\mathbf{q} = \mathbf{Q} - \mathbf{Q}_{\text{stripe}}$. Prior to fitting, the spin gap Δ was first determined by fitting the E (energy) cut at $\mathbf{Q}_{\text{stripe}}$, as shown in Fig. 3(b). This yielded $\Delta = 5.3 \pm 1.5$ meV. The determined spin-wave velocities from the

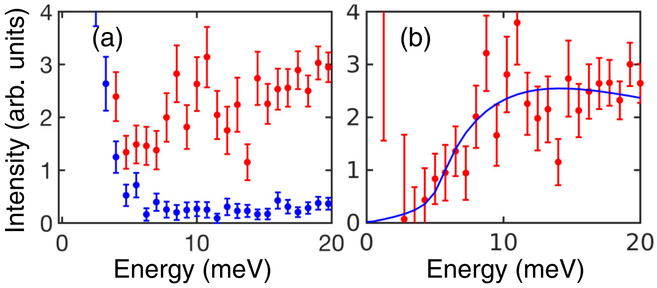

FIG. 3. Energy cuts of data in Fig. 2(g) for $x = 0.026$ at $T = 20$ K. (a) Cuts at $(-0.5, -0.5, -1)$ (red symbols) and $(-0.6, -0.6, -1)$ (blue symbols) obtained by averaging over the LO and TR directions by ±0.05 r.l.u. (b) The cut at $(-0.5, -0.5, -1)$ after subtracting the $(-0.6, -0.6, -1)$ cut and elastic scattering due to the magnetic-Bragg peak. To subtract the Bragg peak, data for $(-0.5, -0.5, -1)$ were fit to a pseudo-Voigt line shape after subtraction of the $(-0.6, -0.6, -1)$ cut. The pseudo-Voigt line shape was then subtracted from the magnetic-scattering data. The blue line is a fit to the model described in Ref. [39] used to determine the spin gap.

TABLE I. Values of the spin gap and spin-wave velocities in the orthorhombic-antiferromagnetic phase. Parameters for $x = 0$ are calculated using exchange constants from Refs. [33,34], whereas those for $x = 0.026$ are from fitting the dispersion data in Figs. 2(h)–2(j) to Eq. (1).

	$x = 0$ Ref. [33]	$x = 0$ Ref. [34]	$x = 0.026$
Δ (meV)	7	6.8	5.3 ± 1.5
υ_{LO} (meV Å)	534	498	520 ± 20
υ_{TR} (meV Å)	386	347	400 ± 17
υ_{c} (meV Å)	246	259	137 ± 4
$\upsilon_{\mathrm{c}}/\upsilon_{\mathrm{LO}}$	0.46	0.52	0.26 ± 0.01

fit to Eq. (1) are listed in Table I, along with corresponding values for $x = 0$.

The fits show that the spin waves in the $x = 0.026$ sample are similar to those in $x = 0$ except for υ_{c}. The smaller ratio of υ_{c} to υ_{LO} for $x = 0.026$ indicates a decrease in the relative strength of the interlayer coupling with Co doping. This signifies an evolution from anisotropic 3D to quasi-two-dimensional (2D) spin excitations with increasing Co doping, similar to $\mathrm{Ba(Fe_{1-\mathit{x}}Co_{\mathit{x}})_2As_2}$ [35]. On the other hand, spin fluctuations in $x \approx 0.040$ $\mathrm{Ba(Fe_{1-\mathit{x}}Co_{\mathit{x}})_2As_2}$ show considerable damping [18], despite having a T_{N} similar to $x = 0.026$ $\mathrm{Ca(Fe_{1-\mathit{x}}Co_{\mathit{x}})_2As_2}$. However, the damping in $x \approx 0.040$ $\mathrm{Ba(Fe_{1-\mathit{x}}Co_{\mathit{x}})_2As_2}$ occurs when there is microscopic coexistence of AFM order and SC [8,18], and such coexsitence is absent for $\mathrm{Ca(Fe_{1-\mathit{x}}Co_{\mathit{x}})_2As_2}$ [20,36]. We therefore surmise that the absence of diffusive spin dynamics in the AFM phase of $x = 0.026$ $\mathrm{Ca(Fe_{1-\mathit{x}}Co_{\mathit{x}})_2As_2}$ is consistent with the absence of coexisting AFM order and SC. This links the presence of diffusive spin dynamics to the existence of SC.

B. Spin fluctuations in the tetragonal-paramagnetic phase at high temperature

We next measured the spin fluctuations in the PM phase at $T = 90$ K for $x = 0.026$ ($T/T_{\mathrm{N}} \approx 1.4$) and $x = 0.030$. E slices along the TR direction and Q slices are shown in Fig. 4 for both samples after subtracting an estimated isotropic background using the method discussed in Ref. [37]. Scattering due to spin fluctuations emanates from $\mathbf{Q}_{\mathbf{stripe}}$, but appears much broader in both E and $\mathbf{Q}$ than the spin-wave scattering in the AFM state. This is due to some combination of a shorter lifetime of the excitations, weaker interlayer interactions, and shorter-range in-plane correlations of the Fe moments. The Q slices also show different broadening along the LO and TR directions which indicates anisotropic in-plane magnetic correlations.

In order to quantify the scattering, we fit the E cuts at $\mathbf{Q}_{\mathbf{stripe}}$ in Fig. 5 and the Q cuts given in Fig. 6 to the diffusive model for the PM state of $\mathrm{CaFe_2As_2}$ discussed in Refs. [25,38]. The model considers anisotropic in-plane correlations along with overdamped dynamics originating from the decay of spin fluctuations into particle-hole excitations. The resulting imaginary part of the dynamical susceptibility is

$$\chi''(\mathbf{Q},E) = \frac{\gamma\chi_0 E}{E^2 + \gamma^2\left\{\left(q_{\mathrm{x}}^2 + q_{\mathrm{y}}^2 + \eta q_{\mathrm{x}} q_{\mathrm{y}}\right)a^2 + \left(\frac{a}{\xi}\right)^2 + \eta_{\mathrm{c}}[1 + \cos(\pi L)]\right\}^2}, \tag{2}$$

where $\mathbf{q} = \mathbf{Q} - \mathbf{Q}_{\mathrm{stripe}}$, $q^2 = q_{\mathrm{x}}^2 + q_{\mathrm{y}}^2 + q_{\mathrm{c}}^2$, x and y are along [1 0 0] and [0 1 0] directions of the tetragonal $I4/mmm$ crystal system, respectively, χ_0 is the staggered susceptibility, γ denotes the damping coefficient originating from decay of spin fluctuations into particle-hole excitations, ξ is the magnetic correlation length in the **ab** plane, η represents the anisotropy of the in-plane magnetic-correlation length, and $\eta_{\mathrm{c}} = J_{\mathrm{c}}\chi_0$ gives the strength of the interlayer spin correlations. The fluctuation dissipation theorem relates the imaginary part of the dynamical susceptibility to the dynamical structure factor by

$$S(\mathbf{Q},E) = (r_0)^2 \frac{f^2(\mathbf{Q})}{2\pi\mu_{\mathrm{B}}^2} \frac{\chi''(\mathbf{Q},E)}{1 - e^{-E/k_{\mathrm{B}}T}}, \tag{3}$$

where $(r_0)^2 = 290.6$ mbarns sr^{-1} and $f(\mathbf{Q})$ is the magnetic form factor for Fe^{2+}. The E and Q cuts in Figs. 5 and 6 were simultaneously fit to Eqs. (2) and (3).

For the fits, η was determined from the width of the Q cuts in the TR and LO directions for $L = 1$ shown in Fig. 6. The Q cuts were fit to a Gaussian line shape, and the corresponding magnetic correlation length was determined from the fitted FWHM, κ, using $\xi \approx \frac{\sqrt{\ln 2}}{\pi}\frac{a}{\kappa}$. η was then determined from the magnetic correlation lengths using the relation [33] $\eta = 2\frac{\xi_{\mathrm{LO}}^2 - \xi_{\mathrm{TR}}^2}{\xi_{\mathrm{LO}}^2 + \xi_{\mathrm{TR}}^2}$ and is kept fixed throughout the fitting.

The protocol for the fits follows. First, the E cuts in Fig. 5 were fit by keeping η_{c} fixed at a value in the range from 0.1 to 0.6. The Lorentzian width [$\Gamma = \gamma(\frac{a}{\xi})^2$] obtained from the fits

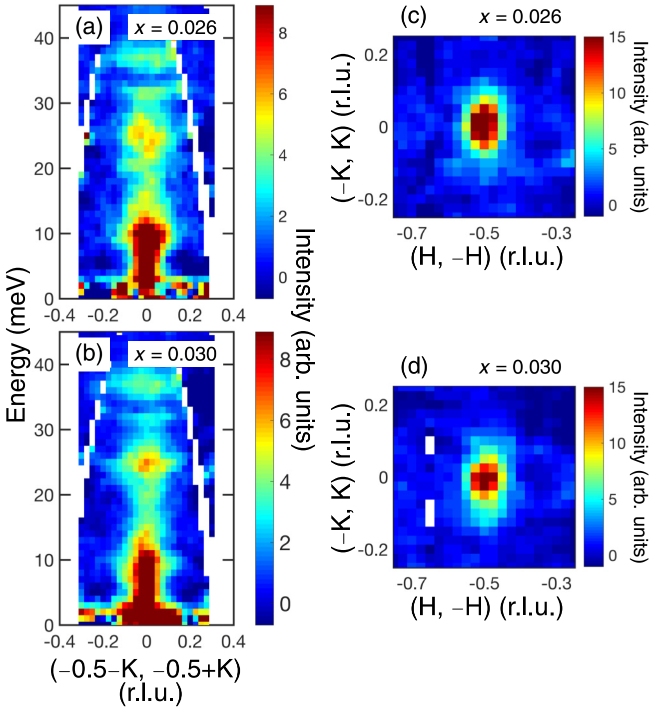

FIG. 4. Paramagnetic spin fluctuations in $x = 0.026$ and 0.030 measured at $T = 90$ K with $E_{\rm i} = 49.75$ meV and c fixed along the incident-beam direction. (a),(b) TR slices of background subtracted data for $(-0.5, -0.5, L)$ averaged over the LO direction by ± 0.06 r.l.u. for $x = 0.026$ and 0.030, respectively. An isotropic background has been estimated and subtracted as discussed in Ref. [37]. (c),(d) Q slices of background subtracted data averaged over $E = 5.5$–9.5 meV ($L \approx 1$), for $x = 0.026$ and 0.030, respectively.

was then kept fixed in subsequent fitting of the Q cuts shown in Fig. 6. Fits of the Q cuts for different values of L and along different directions (LO and TR) produced almost identical values of χ_0 and ξ. Due to the interrelated nature of χ_0 and ξ, the average of χ_0 from all of the fits was then kept fixed to the values in Table II and the data were fit again by varying ξ. During the entire fitting procedure (i.e., for χ_0 fixed and free), ξ is found within ± 0.5 Å of the average value shown in Table II. Finally, the best fit value for $\eta_{\rm c}$ was determined from a χ-squared analysis of results from fits where only $\eta_{\rm c}$ was varied. The results of the fits are listed in Table II along with values for CaFe$_2$As$_2$.

We estimate the size of the fluctuating moment per Fe atom by using the fitted values in Table II and the equation:

$$\langle m^2 \rangle = \frac{1}{2}\frac{3}{\pi}\frac{\int \chi''(\mathbf{Q},E)(1-e^{-E/k_{\rm B}T})^{-1} d\mathbf{Q}\, dE}{\int d\mathbf{Q}}. \tag{4}$$

Here, the integration is done in the orthorhombic zone in order to compare with previous results, and is performed over the ranges $0 \leqslant Q_{\rm x} \leqslant \frac{2\sqrt{2}\pi}{a}$, $\frac{-\sqrt{2}\pi}{a} \leqslant Q_{\rm y} \leqslant \frac{\sqrt{2}\pi}{a}$, and $0 \leqslant Q_z \leqslant \frac{4\pi}{c}$. An upper energy cutoff of 200 meV is used. The determined values for $\sqrt{\langle m^2 \rangle}$ are given in Table II.

The similarity of the values for the fit parameters of $x = 0.030$ and $x = 0.026$ at $T = 90$ K with those for $x = 0$ at $T = 150$ and 180 K shows that the diffusive spin dynamics in

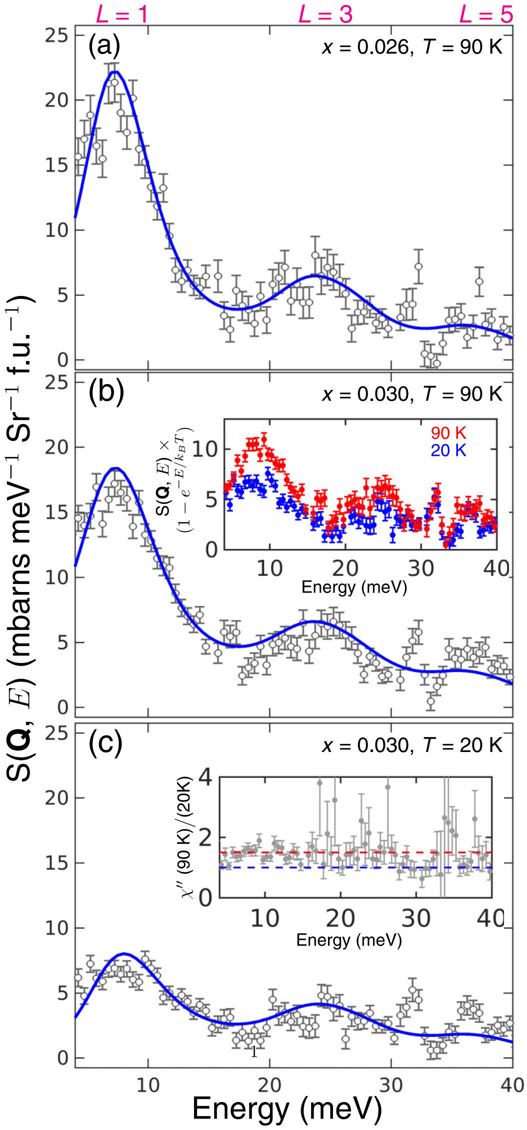

FIG. 5. E cuts at $\mathbf{Q}_{\mathbf{stripe}}$ for $x = 0.026$ at $T = 90$ K (a), and $x = 0.030$ at $T = 90$ (b) and 20 K (c) with $E_{\rm i} = 49.75$ meV. c was fixed along the incident beam direction. Data are subtracted by an isotropic background, similar to Ref. [37], and averaged over ± 0.03 r.l.u. in both the LO and TR directions. Blue lines are fits using the model discussed in the text and fit parameters listed in Tables II and III. The inset to (b) shows E cuts corrected by the Bose-occupation factor for $x = 0.030$ at $T = 90$ (red circles) and 20 K (blue circles). The inset to (c) shows the ratio of the $T = 90$ to 20 K data shown in the inset to (b). The red and blue dashed lines are guides to the eye and indicate ratios of 1.5 and 1.

the PM phase at high temperature are relatively insensitive to Co doping. This is different than the case of Ba(Fe$_{1-x}$Co$_x$)$_2$As$_2$ for which Landau damping (i.e., γ) increases with increasing x [18,37].

C. Spin fluctuations in the tetragonal-paramagnetic and superconducting phases at low temperature

E and Q cuts of INS data showing diffusive spin fluctuations for $x = 0.030$ at $T = 20$ K ($T/T_{\rm c} \approx 1.4$) are given in Figs. 5(c) and 6. The data are qualitatively similar to the $T = 90$ K data,

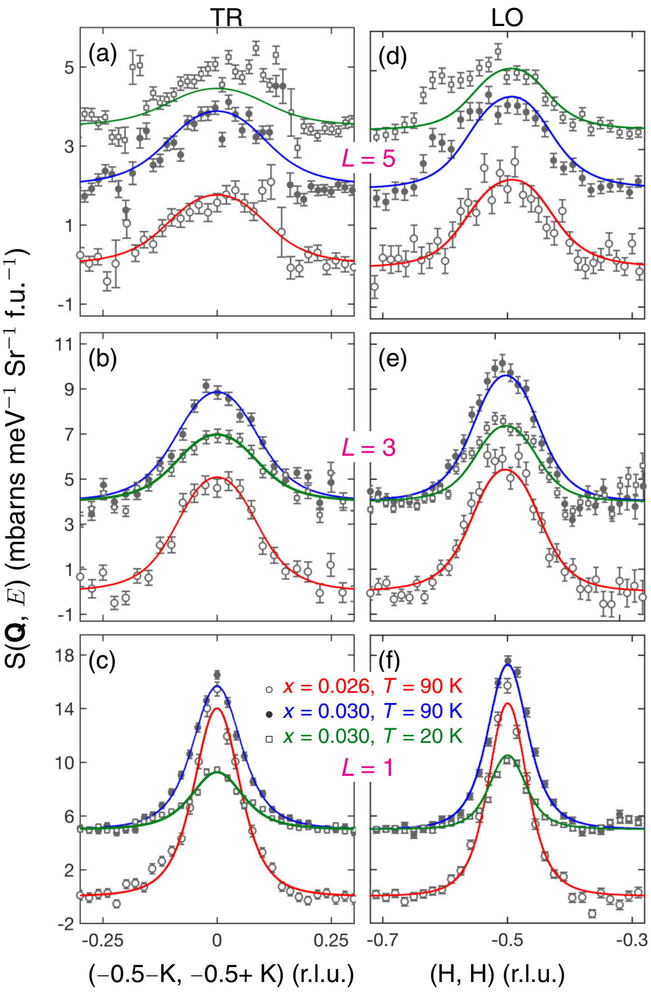

FIG. 6. Q cuts for $x = 0.026$ and 0.030 along the TR [(a)–(c)] and LO [(d)–(f)] directions measured at $T = 90$ and 20 K with $E_{\mathrm{i}} = 49.75$ meV and c fixed along the incident-beam direction. A fitted background has been subtracted and the cuts are taken at energy transfers corresponding to $L = 1, 3$, and 5. TR cuts are averaged over ±0.06, ±0.06, and ±0.10 r.l.u. along the LO direction for $L = 1$, 3, and 5, respectively, and LO cuts are averaged over ±0.08, ±0.08, and ±0.10 r.l.u. along the TR direction for $L = 1$, 3, and 5, respectively. The in-plane anisotropy is apparent from the difference in width between scattering along the LO and TR directions. Red, blue, and green lines are fits using the model discussed in the text with the parameters given in Tables II and III. Cuts for different values of L are offset for clarity.

with the exception of a marked decrease in intensity. The inset of Fig. 5(b) shows data after correcting by the Bose factor and illustrates that χ'' decreases upon cooling down to $T = 20$ K. The inset to Fig. 5(c) presents the ratio of χ'' at $T = 90$ K to that at 20 K and shows that the 20 K data decrease by a scale factor of nearly 1.5 for all energy transfers $E < 30$ meV. Table III shows that the parameters determined from fitting the $T = 20$ K data to the diffusive model compare well with those found for 90 K, except for a decrease in χ_0, which indicates a loss of fluctuating Fe moment. The calculation of the fluctuating Fe moment from these fit values gives $\sqrt{\langle m^2 \rangle} = (0.50 \pm 0.02\mu_{\mathrm{B}})$/Fe, which is a decrease of nearly 21% at 20 K with respect to 90 K. In addition, the similarity of the E and Q cuts shown in Fig. 7 for $T = 20$ and 6 K show that similar spin fluctuations occur in the SC phase as in the normal state (20 K), and that there is no further decrease in intensity for $T < 20$ K. The fluctuating Fe moment of $\sqrt{\langle m^2 \rangle} = (0.47 \pm 0.02\mu_{\mathrm{B}})$/Fe is calculated for $T = 6$ K.

Other iron-arsenide superconductors display a spin-resonance peak below T_{c} due to a redistribution of the spectral weight associated with spin fluctuations [40] and we expect to observe a similar feature in the INS data for $x = 0.030$. Taking $E_{\mathrm{res}} = 4.5k_{\mathrm{B}}T_{\mathrm{c}}$ as the value for the expected resonance energy, as in optimally doped Ba(Fe$_{1-x}$Co$_x$)$_2$As$_2$ [35], the resonance peak is expected at $E \approx 5.4$ meV. However, the measurement performed in the SC state at $T = 6$ K did not find a spin-resonance peak in the measured regions of $\mathbf{Q}$ and E as shown in Fig. 7. The resonance may not be observable due to our experimental configuration, which has the incident beam fixed along c. In this configuration, E and L are coupled, so $E = 5.4$ meV corresponds to $L = 0.77$ for $E_{\mathrm{i}} = 49.75$ meV and $(H,H) = (0.5,0.5)$. This value of L is shifted away from the optimal $L = 1$ position corresponding to $\mathbf{Q}_{\mathrm{stripe}}$ and the stronger 3D character of CaFe$_2$As$_2$ (as compared to BaFe$_2$As$_2$) [2] would strongly suppress the resonance intensity away from $L = 1$. Thus another measurement that accesses lower energy transfers at $\mathbf{Q}_{\mathrm{stripe}}$ is required to make a firm conclusion about the existence of a spin-resonance peak.

IV. DISCUSSION

The results presented above show the following. (1) Spin excitations centered at $\mathbf{Q}_{\mathbf{stripe}}$ occur in the T-PM, O-AFM, and SC phases of Ca(Fe$_{1-x}$Co$_x$)$_2$As$_2$. (2) The low-temperature spin dynamics become more 2D with increasing electron doping up to at least $x = 0.030$. (3) Well-defined gapped spin waves

TABLE II. Parameters of Eq. (2) obtained by fitting INS data for the tetragonal-paramagnetic phase at high temperature, along with the corresponding values for CaFe$_2$As$_2$ from Refs. [25,38]. The last row contains the fluctuating moment per Fe calculated from the parameters.

	$x = 0$ Ref. [38], $T = 180$ K	$x = 0$ Ref. [25], $T = 150$ K	$x = 0.026$ $T = 90$ K	$x = 0.030$ $T = 90$ K
χ_0 (μ_{B}^2 meV^{-1} f.u.$^{-1}$)	0.20 ± 0.05		0.14 ± 0.01	0.15 ± 0.01
η	0.55 ± 0.36	1.0 ± 0.2	0.88 ± 0.14	0.90 ± 0.13
η_{c}	0.20 ± 0.02	0.16 ± 0.02	0.20 ± 0.05	0.16 ± 0.06
Γ (meV)	10.0	14.3 ± 0.8	7.8 ± 0.5	9.8 ± 0.5
γ (meV)	43 ± 5	37 ± 2	41 ± 3	41 ± 3
ξ (Å)	7.9 ± 0.1	6.4 ± 0.2	9.0 ± 0.2	8.0 ± 0.2
$\sqrt{\langle m^2 \rangle}$ (μ_{B}/Fe)	0.71 ± 0.09		0.60 ± 0.02	0.63 ± 0.02

TABLE III. Parameters of Eq. (2) obtained from fitting $T = 90$ and 20 K data for $x = 0.030$.

	$x = 0.030$ $T = 90$ K	$x = 0.030$ $T = 20$ K
χ_0 (μ_{B}^2 meV^{-1} f.u.$^{-1}$)	0.15 ± 0.01	0.09 ± 0.01
η	0.90 ± 0.13	1.12 ± 0.30
Γ (meV)	9.8 ± 0.5	9.5 ± 0.8
γ (meV)	41 ± 3	45 ± 4
ξ (Å)	8.0 ± 0.2	8.5 ± 0.2
$\sqrt{\langle m^2\rangle}$ (μ_{B}/Fe)	0.63 ± 0.02	0.50 ± 0.02

with small damping persist in the O-AFM phase up to at least $x = 0.026$. (4) Similar diffusive spin fluctuations are present in the T-PM phase for both $x = 0.026$ and 0.030 at $T = 90$ K. (5) Similar diffusive spin fluctuations are present in the SC phase of $x = 0.030$ as in the normal T-PM state. (6) For $E < 30$ meV, $\chi''(\mathbf{Q}_{\mathbf{stripe}}, E)$ decreases between $T = 90$ and 20 K for $x = 0.030$. (7) The low-temperature ($T = 20$ K) spin dynamics changes abruptly between O-AFM $x = 0.026$ and T-PM $x = 0.030$, where the change in x is only 0.004, consistent with the strong–first order line separating O-AFM and other phases in Ca(Fe$_{1-x}$Co$_x$)$_2$As$_2$. We now compare these results with those for the closely related electron-doped series Ba(Fe$_{1-x}$Co$_x$)$_2$As$_2$. Descriptions of the spin dynamics in other related compounds are found in, for example, Ref. [41].

Similar to Ca(Fe$_{1-x}$Co$_x$)$_2$As$_2$, spin excitations centered at $\mathbf{Q}_{\mathbf{stripe}}$ are found in the T-PM, O-AFM, and SC phases of Ba(Fe$_{1-x}$Co$_x$)$_2$As$_2$ [37,40,42,43] and the spin dynamics become more 2D with increasing x [18]. However, AFM order and SC microscopically coexist in underdoped Ba(Fe$_{1-x}$Co$_x$)$_2$As$_2$ over $0.04 \lesssim x \lesssim 0.06$ [44,45], with the appearance of SC being coincident with an increase in the damping of spin excitations [18]. As x is increased through the coexistence region, connecting O-AFM and SC phases, a crossover from the well-defined spin waves to the diffusive spin fluctuations occurs [18]. Since Ca(Fe$_{1-x}$Co$_x$)$_2$As$_2$ does not possess a region of microscopically coexisting AFM order and SC, one may expect that the crossover to diffusive spin fluctuations found for Ba(Fe$_{1-x}$Co$_x$)$_2$As$_2$ is absent.

The results presented above are consistent with this expectation, as our data show that well-defined spin waves persist in the AFM phase of Ca(Fe$_{1-x}$Co$_x$)$_2$As$_2$ up to at least $x = 0.026$. We can go one step further by considering that T_{N} for $x = 0.026$ is similar to T_{N} for $x \approx 0.040$ Ba(Fe$_{1-x}$Co$_x$)$_2$As$_2$, which displays diffusive spin dynamics. Thus, despite a similar characteristic energy for the AFM order in both of these compounds, their magnetic-excitation spectra are inherently different, with the striking physical difference between the two compounds being the presence of SC.

Analysis of INS data for Ba(Fe$_{1-x}$Co$_x$)$_2$As$_2$ also infers that the crossover from well-defined spin waves to diffusive spin fluctuations with increasing x in its O-AFM phase is concomitant with a suppression of the spin-density-wave gap Δ_{SDW} associated with the itinerant AFM order [18]. Since Δ_{SDW} is proportional to the ordered-magnetic moment μ [18,46], changes in μ should reflect changes to Δ_{SDW} and the size of μ can be used as a determining factor for the appearance of diffusive spin dynamics. μ for Ba(Fe$_{1-x}$Co$_x$)$_2$As$_2$ decreases from 0.87 to $\approx 0.1\mu_{\mathrm{B}}$/Fe as the composition is varied from $x = 0$ to 0.059 [44,45], which is near the O-AFM to SC phase boundary. On the other hand, μ for Ca(Fe$_{1-x}$Co$_x$)$_2$As$_2$ changes very little across the O-AFM phase, decreasing from $\mu = 0.8\mu_{\mathrm{B}}$/Fe for $x = 0$ to $\mu = 0.71\mu_{\mathrm{B}}$/Fe for $x = 0.028$ [47], which is near the first-order phase boundary. Hence the change in Δ_{SDW} across the O-AFM phase of Ca(Fe$_{1-x}$Co$_x$)$_2$As$_2$ should be much less than for Ba(Fe$_{1-x}$Co$_x$)$_2$As$_2$, which supports the notion that well-defined spin waves persist throughout the O-AFM state of Ca(Fe$_{1-x}$Co$_x$)$_2$As$_2$.

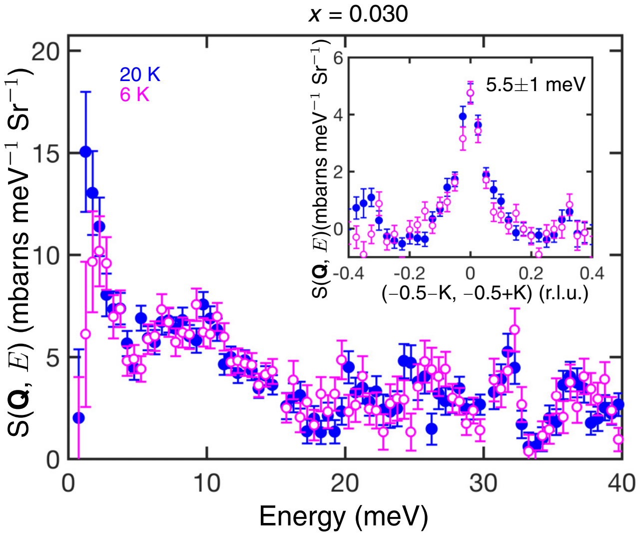

FIG. 7. E cuts at $\mathbf{Q}_{\mathbf{stripe}}$ for $x = 0.030$ measured at $T = 20$ (filled circle) and 6 K (open circle) with $E_{\mathrm{i}} = 49.75$ meV and c fixed along the incident-beam direction. Data are subtracted by an isotropic background, similar to Ref. [37], and averaged over ±0.03 r.l.u. in both the LO and TR directions. The inset shows Q cuts along the TR direction obtained after averaging over $E = 4.5$–6.5 meV and along the LO direction by ±0.05. Data for $E \lesssim 4$ meV are dominated by incoherent scattering.

The negligible changes in damping of the spin fluctuations in the T-PM phase of Ca(Fe$_{1-x}$Co$_x$)$_2$As$_2$ with increasing x is in contrast to the sizable increase in damping of the fluctuations seen for Ba(Fe$_{1-x}$Co$_x$)$_2$As$_2$ [18,37]. This difference can be understood in terms of changes to the electronic-band structure due to electron doping. In particular, the shrinking (expansion) of hole (electron) pockets due to the addition of electrons changes the Fermi velocities of electrons and holes connected by $\mathbf{Q}_{\mathbf{stripe}}$, resulting in an increase in damping in Ba(Fe$_{1-x}$Co$_x$)$_2$As$_2$ [18]. Since the number of electrons introduced into optimally doped Ca(Fe$_{1-x}$Co$_x$)$_2$As$_2$ is nearly half that for optimally doped Ba(Fe$_{1-x}$Co$_x$)$_2$As$_2$ [9], the almost constant value of the damping parameter in the T-PM phase of Ca(Fe$_{1-x}$Co$_x$)$_2$As$_2$ for $x \leqslant 0.030$ may be the result of smaller changes to its Fermi surface between $x = 0$ and its optimal-doping level.

Similar to Ca(Fe$_{1-x}$Co$_x$)$_2$As$_2$, diffusive spin fluctuations are found for the T-PM and SC phases of Ba(Fe$_{1-x}$Co$_x$)$_2$As$_2$. We have already discussed in Sec. III C the limitations of our experimental setup in regards to being able to determine whether or not a spin-resonance peak exists in the SC phase.

We next consider the decrease in $\chi''(\mathbf{Q}_{\mathbf{stripe}},E)$, for $4 \lesssim E < 30$ meV, with decreasing temperature in the T-PM phase of $x = 0.030$ $Ca(Fe_{1-x}Co_x)_2As_2$.

The decrease in $\chi''(\mathbf{Q}_{\mathbf{stripe}},E)$ at low energies contrasts with previous results for the T-PM states of $CaFe_2As_2$ [38] and $Ba(Fe_{1-x}Co_x)_2As_2$ [40,48], where $\chi''(\mathbf{Q}_{\mathbf{stripe}},E)$ generally increases with decreasing temperature. In the T-PM phases of $CaFe_2As_2$ [38] and $Ba(Fe_{1-x}Co_x)_2As_2$ [40,48], the magnetic-correlation length in the ab plane increases with decreasing temperature, whereas we find it to be relatively unchanged for $Ca(Fe_{0.97}Co_{0.03})_2As_2$. We find that the decrease of $\chi''(\mathbf{Q}_{\mathbf{stripe}},E)$ at low energies with decreasing temperature for $Ca(Fe_{0.97}Co_{0.03})_2As_2$ is associated with a decrease in the magnitude of the fluctuating Fe moment. Nuclear magnetic resonance (NMR) measurements have also observed a suppression of AFM spin fluctuations in the normal state of SC samples of $Ca(Fe_{1-x}Co_x)_2As_2$ below a temperature T^*, which is attributed to the opening of a pseudogap [47].

Timusk and Statt define the pseudogap as a partial gapping of the Fermi surface [49], and many theories have been put forth that describe the origin of the pseudogap found for certain high-T_c cuprate superconductors [50,51]. Among the theories is the case of preformed Cooper pairs, which suggests that the pairing necessary for SC starts at a temperature $T^* > T_c$. NMR data provided the first experimental evidence for the pseudogap in $YBa_2Cu_3O_{6.7}$ by showing a suppression of the spin-lattice relaxation rate below T^* [52,53]. INS measurements have observed the development of a spin resonance at $T^* > T_c$, which is associated with the opening of a pseudogap [51,54].

Signatures of a pseudogap phase are also observed for some iron-arsenide superconductors. For example, a spin-resonance peak is found for $(CaFe_{1-x}Pt_xAs)_{10}Pt_3As_8$ above T_c [55]. Further, the spin-resonance peak occurs at the same values of E for $T^* > T > T_c$ and $T < T_c$, for both the cuprate [56] and iron-arsenide [55] superconductors, and, generally, the magnetic-scattering intensity at values of E lower than the resonance peak is suppressed. In contrast, we find a suppression of $\chi''(\mathbf{Q}_{\mathbf{stripe}},E)$ for $Ca(Fe_{0.97}Co_{0.03})_2As_2$ at values of E much larger than the expected resonance energy of $E_{res} \approx 5.4$ meV, which differs with previous results for materials displaying a pseudogap [55,56]. However, as noted above, INS measurements specifically targeting lower values of E at positions corresponding to $\mathbf{Q}_{\mathbf{stripe}}$ are required to make a firm conclusion about the existence of a spin-resonance peak in $Ca(Fe_{0.97}Co_{0.03})_2As_2$.

Another potential explanation for the decrease in the fluctuating Fe moment lies with the proximity of the $x = 0.030$ sample to the cT phase found for $CaFe_2As_2$ [21,22] and related compounds [57,58]. As discussed in Sec. I, the cT phase of $CaFe_2As_2$ is characterized by a decrease in c of ≈9.5%, with $c = 10.607$ Å in the cT phase at $T = 50$ K [21], and quenching of the Fe magnetic moment [21,24,25]. Figure 1(d) shows that c for $x = 0.030$ decreases with decreasing temperature, moving towards the cT phase. If we associate the approach to the cT phase with an increase in the interlayer As-As hybridization [26,58–62], then it is possible that the Fe magnetic moment is concomitantly decreasing. Such an effect is shown to be the case for $CaFe_2(As_{1-x}P_x)_2$, $x = 0.033$ and 0.055, and $Ca_{0.78}La_{0.22}Fe_2As_2$ [63,64]. Thus we suggest that the suppression of $\chi''(\mathbf{Q}_{\mathbf{stripe}},E)$ with decreasing temperature for $Ca(Fe_{0.97}Co_{0.03})_2As_2$ may be due to a decrease in Fe moment tied to the decrease in c. No such suppression in $\chi''(\mathbf{Q}_{\mathbf{stripe}},E)$ is observed for $x = 0.026$ between $T = 90$ and 20 K, because c increases only weakly upon cooling through $T_{S,N}$, as shown in Fig. 1(d). In fact, for both $CaFe_2As_2$ and $CaFe_2(As_{0.967}P_{0.033})_2$, c increases weakly upon cooling through $T_{S,N}$ and corresponding to this the local Fe magnetic moment is found to be increased [64].

V. CONCLUSION

We have presented detailed results of the spin dynamics in $Ca(Fe_{1-x}Co_x)_2As_2$ for values of x straddling the first-order AFM to SC phase boundary. These results share similar characteristics to other 122-iron-arsenide compounds, but also emphasize key differences that are consistent with its unique properties. In particular, the existence of well-defined spin waves up to $x = 0.026$ appears to rule out a crossover region from well-defined spin-wave-type to diffusive-type spin dynamics in the O-AFM phase, as found for $Ba(Fe_{1-x}Co_x)_2As_2$. We have discussed the implications of this result in terms of the absence of microscopically coexisting AFM order and SC. In addition, we have shown a peculiar decrease with decreasing temperature of the imaginary part of the low-energy dynamic magnetic susceptibility for $Ca(Fe_{0.97}Co_{0.03})_2As_2$, which we propose is due to decrease in the Fe magnetic moment associated with either the opening of a pseudogap or the proximity to the cT phase. Further experiments are necessary to either confirm or rule out the presence of a pseudogap as well as the existence of a spin-resonance peak in INS data.

ACKNOWLEDGMENTS

We are grateful for the assistance of Yuji Furukawa (Ames Laboratory), Jong Keum (X-ray Laboratory, SNS, ORNL), and Louis J. Santodonato (CG-1B, HFIR, ORNL). Work at the Ames Laboratory was supported by U.S. Department of Energy, Basic Energy Sciences, Division of Material Sciences and Engineering, under Contract No. DE-AC02-07CH11358. This research used resources at the Spallation Neutron Source, a DOE Office of Science User Facility operated by the Oak Ridge National Laboratory.

APPENDIX

1. Convolution with instrumental resolution

The data in Fig. 2(g) from which the dispersion along $[0,0,L]$ is determined do not show two resolvable spin-wave branches. This is due to the instrumental resolution. To account for broadening due to the resolution, we fit the peak in a Q cut of data from Fig. 2(g) to a Gaussian line shape convoluted with another Gaussian line shape that represents the instrumental resolution. The FWHM of the Gaussian line shape for the resolution is calculated using [65]

$$\delta Q = \frac{1}{Q}\left[Q_{\mathrm{x}}^2(\delta Q_{\mathrm{x}})^2 + Q_{\mathrm{y}}^2(\delta Q_{\mathrm{y}})^2\right]^{1/2}, \tag{A1}$$

where

$$\begin{aligned}\delta Q_{\mathrm{x}} = \frac{m_n}{\hbar}\Bigg\{&\frac{1}{L_1^2}\left(v_i^2 + v_f^2\frac{L_2}{L_3}\cos 2\theta\right)^2\delta t_p^2\\ &+\frac{1}{L_1^2}\left(v_i^2 + v_f^2\frac{L_1+L_2}{L_3}\cos 2\theta\right)^2\delta t_{\mathrm{c}}^2\\ &+\left(\frac{v_f^2}{L_3}\cos 2\theta\right)^2\delta t_d^2 + (v_f\sin 2\theta)^2(\delta 2\theta)^2\Bigg\}^{1/2}\end{aligned}$$

and

$$\begin{aligned}\delta Q_{\mathrm{y}} = \frac{m_n}{\hbar}\Bigg\{&\left(\frac{v_f^2 L_2}{L_1 L_3}\sin 2\theta\right)^2\delta t_p^2 + \left(\frac{v_f^2}{L_1}\frac{L_1+L_2}{L_3}\sin 2\theta\right)^2\delta t_{\mathrm{c}}^2\\ &+\left(\frac{v_f^2}{L_3}\sin 2\theta\right)^2\delta t_d^2 + (v_f\cos 2\theta)^2(\delta 2\theta)^2\Bigg\}^{1/2}.\end{aligned}$$

Here, δQ, $\delta Q_{x,y}$, Q, and $Q_{x,y}$ have units of Å^{-1}, v_i and v_f are initial and final velocities of the neutron, L_1, L_2, and L_3 are the distances from the moderator to the Fermi chopper, the Fermi chopper to the sample, and the sample to the detector, respectively, and δt_p, δt_{c}, and δt_d are time spreads associated with neutron travel through the moderator and Fermi chopper, and the uncertainty associated with the sample position, respectively. Here, x and y represent the direction parallel and perpendicular to the incident beam direction. We take the sample width to be 3 cm, which approximates the extent of the coaligned single-crystal sample. Values of the resolution δQ for data at (0.5,0.5,1) and (0.5,0.5,3) are shown in Table IV.

TABLE IV. Instrumental resolution δQ for Q cuts centered at (0.5,0.5,1) for E up to 23.5 meV and (0.5,0.5,3) for E up to 30 meV, with $E_{\mathrm{i}} = 73.9$ meV.

E (meV)	9	13.5	18.5	23.5	30
δQ (Å^{-1})	0.08	0.08	0.08	0.09	0.08

Using the corresponding value of δQ given in Table IV as the width of the Gaussian line shape representing the instrumental resolution, a peak in a Q cut is fit to

$$I(q) = \frac{A}{2\pi\sigma_1\sigma_2}\int_{-\infty}^{\infty} e^{-q^2/2\sigma_1^2}e^{-(q'-q)^2/2\sigma_2^2}\,dq', \tag{A2}$$

where I is the neutron-scattering intensity and σ_1 and σ_2 represent the standard deviation of the peak corresponding to the signal of interest and the instrumental resolution, respectively.

2. Procedure to obtain values of *L* for the measurements where incident energy is fixed along the *c* direction

For the data where the incident beam was fixed along the c, the variables in the four-dimensional $(E,\mathbf{Q})$ space are coupled. Here, $\mathbf{Q} = (Q_x, Q_y, Q_z)$, where $\mathbf{Q}_x = \frac{2\pi}{a}H\hat{\mathbf{i}}$, $\mathbf{Q}_y = \frac{2\pi}{a}K\hat{\mathbf{j}}$, and $\mathbf{Q}_z = \frac{2\pi}{c}L\hat{\mathbf{k}}$. The incident beam is fixed along $\mathbf{Q}_z$ direction. All the figures, both the contour plots and one-dimensional cuts, that are discussed in the main text have Q_z (or L) coupled to (E, Q_x, Q_y). To obtain the values of Q_z (and L) corresponding to (E, Q_x, Q_y), the basic equation of the scattering, conservation of angular momentum, and conservation of energy are solved,

$$\mathbf{Q} = \mathbf{k}_{\mathrm{i}} - \mathbf{k}_{\mathrm{f}}, \tag{A3}$$

$$E = E_{\mathrm{i}} - E_{\mathrm{f}}. \tag{A4}$$

Here, E_{i}, E_{f}, k_{i}, and k_{f} are incident energy, final energy, incident wave vector, and final wave vector of neutron, respectively. After solving Eqs. (A3) and (A4), we get the following relationship for the case where neutron loses energy:

$$Q_z = k_{\mathrm{i}} - \sqrt{k_{\mathrm{f}}^2 - Q_x^2 - Q_y^2}. \tag{A5}$$

From Q_z, the value of L is obtained.

---

[1] P. C. Canfield and S. L. Bud'ko, Annu. Rev. Condens. Matter Phys. **1**, 27 (2010).

[2] D. C. Johnston, Adv. Phys. **59**, 803 (2010).

[3] G. R. Stewart, Rev. Mod. Phys. **83**, 1589 (2011).

[4] N. Ni, S. Nandi, A. Kreyssig, A. I. Goldman, E. D. Mun, S. L. Bud'ko, and P. C. Canfield, Phys. Rev. B **78**, 014523 (2008).

[5] J.-Q. Yan, A. Kreyssig, S. Nandi, N. Ni, S. L. Bud'ko, A. Kracher, R. J. McQueeney, R. W. McCallum, T. A. Lograsso, A. I. Goldman, and P. C. Canfield, Phys. Rev. B **78**, 024516 (2008).

[6] M. G. Kim, R. M. Fernandes, A. Kreyssig, J. W. Kim, A. Thaler, S. L. Bud'ko, P. C. Canfield, R. J. McQueeney, J. Schmalian, and A. I. Goldman, Phys. Rev. B **83**, 134522 (2011).

[7] M. D. Lumsden and A. D. Christianson, J. Phys.: Condens. Matter **22**, 203203 (2010).

[8] N. Ni, M. E. Tillman, J.-Q. Yan, A. Kracher, S. T. Hannahs, S. L. Bud'ko, and P. C. Canfield, Phys. Rev. B **78**, 214515 (2008).

[9] S. Nandi, M. G. Kim, A. Kreyssig, R. M. Fernandes, D. K. Pratt, A. Thaler, N. Ni, S. L. Bud'ko, P. C. Canfield, J. Schmalian, R. J. McQueeney, and A. I. Goldman, Phys. Rev. Lett. **104**, 057006 (2010).

[10] M. Rotter, M. Tegel, and D. Johrendt, Phys. Rev. Lett. **101**, 107006 (2008).

[11] A. Leithe-Jasper, W. Schnelle, C. Geibel, and H. Rosner, Phys. Rev. Lett. **101**, 207004 (2008).

[12] L. Harnagea, S. Singh, G. Friemel, N. Leps, D. Bombor, M. Abdel-Hafiez, A. U. B. Wolter, C. Hess, R. Klingeler, G. Behr, S. Wurmehl, and B. Büchner, Phys. Rev. B **83**, 094523 (2011).

[13] W. Yu, A. A. Aczel, T. J. Williams, S. L. Bud'ko, N. Ni, P. C. Canfield, and G. M. Luke, Phys. Rev. B **79**, 020511 (2009).

[14] E. Colombier, S. L. Bud'ko, N. Ni, and P. C. Canfield, Phys. Rev. B **79**, 224518 (2009).

[15] M. S. Torikachvili, S. L. Bud'ko, N. Ni, and P. C. Canfield, Phys. Rev. Lett. **101**, 057006 (2008).

[16] W. Uhoya, A. Stemshorn, G. Tsoi, Y. K. Vohra, A. S. Sefat, B. C. Sales, K. M. Hope, and S. T. Weir, Phys. Rev. B **82**, 144118 (2010).

[17] W. O. Uhoya, J. M. Montgomery, G. M. Tsoi, Y. K. Vohra, M. A. McGuire, A. S. Sefat, B. C. Sales, and S. T. Weir, J. Phys.: Condens. Matter **23**, 122201 (2011).

[18] G. S. Tucker, R. M. Fernandes, D. K. Pratt, A. Thaler, N. Ni, K. Marty, A. D. Christianson, M. D. Lumsden, B. C. Sales, A. S. Sefat, S. L. Bud'ko, P. C. Canfield, A. Kreyssig, A. I. Goldman, and R. J. McQueeney, Phys. Rev. B **89**, 180503 (2014).

[19] A. I. Goldman, D. N. Argyriou, B. Ouladdiaf, T. Chatterji, A. Kreyssig, S. Nandi, N. Ni, S. L. Bud'ko, P. C. Canfield, and R. J. McQueeney, Phys. Rev. B **78**, 100506 (2008).

[20] S. Ran, S. L. Bud'ko, W. E. Straszheim, J. Soh, M. G. Kim, A. Kreyssig, A. I. Goldman, and P. C. Canfield, Phys. Rev. B **85**, 224528 (2012).

[21] A. Kreyssig, M. A. Green, Y. Lee, G. D. Samolyuk, P. Zajdel, J. W. Lynn, S. L. Bud'ko, M. S. Torikachvili, N. Ni, S. Nandi, J. B. Leão, S. J. Poulton, D. N. Argyriou, B. N. Harmon, R. J. McQueeney, P. C. Canfield, and A. I. Goldman, Phys. Rev. B **78**, 184517 (2008).

[22] A. I. Goldman, A. Kreyssig, K. Prokeš, D. K. Pratt, D. N. Argyriou, J. W. Lynn, S. Nandi, S. A. J. Kimber, Y. Chen, Y. B. Lee, G. Samolyuk, J. B. Leão, S. J. Poulton, S. L. Bud'ko, N. Ni, P. C. Canfield, B. N. Harmon, and R. J. McQueeney, Phys. Rev. B **79**, 024513 (2009).

[23] S. Ran, S. L. Bud'ko, W. E. Straszheim, and P. C. Canfield, Phys. Rev. B **90**, 054501 (2014).

[24] T. Yildirim, Phys. Rev. Lett. **102**, 037003 (2009).

[25] J. H. Soh, G. S. Tucker, D. K. Pratt, D. L. Abernathy, M. B. Stone, S. Ran, S. L. Bud'ko, P. C. Canfield, A. Kreyssig, R. J. McQueeney, and A. I. Goldman, Phys. Rev. Lett. **111**, 227002 (2013).

[26] R. Hoffman and C. Zheng, J. Phys. Chem. **89**, 4175 (1985).

[27] S. L. Bud'ko, S. Ran, and P. C. Canfield, Phys. Rev. B **88**, 064513 (2013).

[28] R. Mittal, L. Pintschovius, D. Lamago, R. Heid, K.-P. Bohnen, D. Reznik, S. L. Chaplot, Y. Su, N. Kumar, S. K. Dhar, A. Thamizhavel, and T. Brueckel, Phys. Rev. Lett. **102**, 217001 (2009).

[29] A. E. Böhmer, A. Sapkota, A. Kreyssig, S. L. Bud'ko, G. Drachuck, S. M. Saunders, A. I. Goldman, and P. C. Canfield, Phys. Rev. Lett. **118**, 107002 (2017).

[30] D. L. Abernathy, M. B. Stone, M. J. Loguillo, M. S. Lucas, O. Delaire, X. Tang, J. Y. Y. Lin, and B. Fultz, Rev. Sci. Instrum. **83**, 015114 (2012).

[31] http://mslice.isis.rl.ac.uk, developed by Radu Coldea, 1998–2001 and ISIS addons and enhancements, 2001–2014.

[32] R. A. Ewings, A. Buts, M. D. Le, J. van Duijn, I. Bustinduy, and T. G. Perring, Nucl. Instrum. Methods, Phys. Res. A **834**, 132 (2016).

[33] S. O. Diallo, V. P. Antropov, T. G. Perring, C. Broholm, J. J. Pulikkotil, N. Ni, S. L. Bud'ko, P. C. Canfield, A. Kreyssig, A. I. Goldman, and R. J. McQueeney, Phys. Rev. Lett. **102**, 187206 (2009).

[34] J. Zhao, D. T. Adroja, D.-X. Yao, R. Bewley, S. Li, X. F. Wang, G. Wu, X. H. Chen, J. Hu, and P. Dai, Nat. Phys. **5**, 555 (2009).

[35] M. D. Lumsden, A. D. Christianson, D. Parshall, M. B. Stone, S. E. Nagler, G. J. MacDougall, H. A. Mook, K. Lokshin, T. Egami, D. L. Abernathy, E. A. Goremychkin, R. Osborn, M. A. McGuire, A. S. Sefat, R. Jin, B. C. Sales, and D. Mandrus, Phys. Rev. Lett. **102**, 107005 (2009).

[36] S. Ran, S. L. Bud'ko, D. K. Pratt, A. Kreyssig, M. G. Kim, M. J. Kramer, D. H. Ryan, W. N. Rowan-Weetaluktuk, Y. Furukawa, B. Roy, A. I. Goldman, and P. C. Canfield, Phys. Rev. B **83**, 144517 (2011).

[37] G. S. Tucker, R. M. Fernandes, H.-F. Li, V. Thampy, N. Ni, D. L. Abernathy, S. L. Bud'ko, P. C. Canfield, D. Vaknin, J. Schmalian, and R. J. McQueeney, Phys. Rev. B **86**, 024505 (2012).

[38] S. O. Diallo, D. K. Pratt, R. M. Fernandes, W. Tian, J. L. Zarestky, M. Lumsden, T. G. Perring, C. L. Broholm, N. Ni, S. L. Bud'ko, P. C. Canfield, H.-F. Li, D. Vaknin, A. Kreyssig, A. I. Goldman, and R. J. McQueeney, Phys. Rev. B **81**, 214407 (2010).

[39] M. Ramazanoglu, A. Sapkota, A. Pandey, J. Lamsal, D. L. Abernathy, J. L. Niedziela, M. B. Stone, A. Kreyssig, A. I. Goldman, D. C. Johnston, and R. J. McQueeney, Phys. Rev. B **95**, 224401 (2017).

[40] D. S. Inosov, J. T. Park, P. Bourges, D. L. Sun, Y. Sidis, A. Schneidewind, K. Hradil, D. Haug, C. T. Lin, B. Keimer, and V. Hinkov, Nat. Phys. **6**, 178 (2010).

[41] P. Dai, Rev. Mod. Phys. **87**, 855 (2015).

[42] R. A. Ewings, T. G. Perring, R. I. Bewley, T. Guidi, M. J. Pitcher, D. R. Parker, S. J. Clarke, and A. T. Boothroyd, Phys. Rev. B **78**, 220501 (2008).

[43] K. Matan, R. Morinaga, K. Iida, and T. J. Sato, Phys. Rev. B **79**, 054526 (2009).

[44] D. K. Pratt, W. Tian, A. Kreyssig, J. L. Zarestky, S. Nandi, N. Ni, S. L. Bud'ko, P. C. Canfield, A. I. Goldman, and R. J. McQueeney, Phys. Rev. Lett. **103**, 087001 (2009).

[45] R. M. Fernandes, D. K. Pratt, W. Tian, J. Zarestky, A. Kreyssig, S. Nandi, M. G. Kim, A. Thaler, N. Ni, P. C. Canfield, R. J. McQueeney, J. Schmalian, and A. I. Goldman, Phys. Rev. B **81**, 140501 (2010).

[46] R. M. Fernandes and J. Schmalian, Phys. Rev. B **82**, 014521 (2010).

[47] J. Cui, B. Roy, M. A. Tanatar, S. Ran, S. L. Bud'ko, R. Prozorov, P. C. Canfield, and Y. Furukawa, Phys. Rev. B **92**, 184504 (2015).

[48] K. Matan, S. Ibuka, R. Morinaga, S. Chi, J. W. Lynn, A. D. Christianson, M. D. Lumsden, and T. J. Sato, Phys. Rev. B **82**, 054515 (2010).

[49] T. Timusk and B. Statt, Rep. Prog. Phys. **62**, 61 (1999).

[50] M. R. Norman, D. Pines, and C. Kallin, Adv. Phys. **54**, 715 (2005).

[51] A. A. Kordyuk, Low Temp. Phys. **41**, 319 (2015).

[52] W. W. Warren, R. E. Walstedt, G. F. Brennert, R. J. Cava, R. Tycko, R. F. Bell, and G. Dabbagh, Phys. Rev. Lett. **62**, 1193 (1989).

[53] R. E. Walstedt, W. W. Warren, R. F. Bell, R. J. Cava, G. P. Espinosa, L. F. Schneemeyer, and J. V. Waszczak, Phys. Rev. B **41**, 9574 (1990).

[54] C. Stock, W. J. L. Buyers, R. Liang, D. Peets, Z. Tun, D. Bonn, W. N. Hardy, and R. J. Birgeneau, Phys. Rev. B **69**, 014502 (2004).

[55] M. A. Surmach, F. Brückner, S. Kamusella, R. Sarkar, P. Y. Portnichenko, J. T. Park, G. Ghambashidze, H. Luetkens, P. K. Biswas, W. J. Choi, Y. I. Seo, Y. S. Kwon, H.-H. Klauss, and D. S. Inosov, Phys. Rev. B **91**, 104515 (2015).

[56] P. Dai, H. A. Mook, R. D. Hunt, and F. Dogan, Phys. Rev. B **63**, 054525 (2001).

[57] W. T. Jayasekara, U. S. Kaluarachchi, B. G. Ueland, A. Pandey, Y. B. Lee, V. Taufour, A. Sapkota, K. Kothapalli, N. S. Sangeetha, G. Fabbris, L. S. I. Veiga, Y. Feng, A. M. dos Santos, S. L. Bud'ko, B. N. Harmon, P. C. Canfield, D. C. Johnston, A. Kreyssig, and A. I. Goldman, Phys. Rev. B **92**, 224103 (2015).

[58] W. T. Jayasekara, A. Pandey, A. Kreyssig, N. S. Sangeetha, A. Sapkota, K. Kothapalli, V. K. Anand, W. Tian, D. Vaknin, D. C. Johnston, R. J. McQueeney, A. I. Goldman, and B. G. Ueland, Phys. Rev. B **95**, 064425 (2017).

[59] M. Reehuis and W. Jeitschko, J. Phys. Chem. Solids **51**, 961 (1990).

[60] M. Reehuis, W. Jeitschko, G. Kotzyba, B. Zimmer, and X. Hu, J. Alloys Compd. **266**, 54 (1998).

[61] V. K. Anand, P. K. Perera, A. Pandey, R. J. Goetsch, A. Kreyssig, and D. C. Johnston, Phys. Rev. B **85**, 214523 (2012).

[62] V. K. Anand, R. S. Dhaka, Y. Lee, B. N. Harmon, A. Kaminski, and D. C. Johnston, Phys. Rev. B **89**, 214409 (2014).

[63] H. Gretarsson, S. R. Saha, T. Drye, J. Paglione, J. Kim, D. Casa, T. Gog, W. Wu, S. R. Julian, and Y.-J. Kim, Phys. Rev. Lett. **110**, 047003 (2013).

[64] L. Ortenzi, H. Gretarsson, S. Kasahara, Y. Matsuda, T. Shibauchi, K. D. Finkelstein, W. Wu, S. R. Julian, Y.-J. Kim, I. I. Mazin, and L. Boeri, Phys. Rev. Lett. **114**, 047001 (2015).

[65] G. Ehlers, A. A. Podlesnyak, J. L. Niedziela, E. B. Iverson, and P. E. Sokol, Rev. Sci. Instrum. **82**, 085108 (2011).